https://doi.org/10.5194/egusphere-2026-1493
Preprint. Discussion started: 8 April 2026

The first offline land carbon simulation over Europe driven by the atmospheric forcing of a global storm-resolving climate model

Junhong Lee[1,*] and Cathy Hohenegger[1]

[1]Max Planck Institute for Meteorology, Hamburg, Germany
[*]Current affiliation: Climate Prediction Research Center, Seoul National University, Seoul, Republic of Korea

Correspondence: Junhong Lee (junhong.lee@mpimet.mpg.de; junhonglee89@gmail.com)

Abstract. This study is motivated by the hypothesis that the drizzle problem of coarse-resolution climate models, whereby convective precipitation preferentially falls as light precipitation rather than short-lived and intense storms, leads to low gross primary productivity (GPP). To test this hypothesis, we perform an offline land carbon simulation over Europe using a terrestrial biosphere model driven by atmospheric forcing from a global km-scale climate simulation with explicitly resolved convection. This simulation is compared with a coarse-resolution simulation derived by atmospheric forcing from a coarse-resolution climate model with parameterized convection. The km-scale forcing leads, on average, to higher GPP. We find that shorter, more intense daily precipitation events when convection is explicitly resolved allow for stronger downward shortwave radiation on rainy days, thereby enhancing photosynthesis. At the same time, differences in the precipitation climatology between the two atmospheric forcing datasets, with a deficit of precipitation over eastern Europe in the km-scale forcing, result in soil moisture falling below the wilting point and reduced GPP in that region. Consistent with these GPP changes, autotrophic respiration is larger in the km-scale simulation, whereas heterotrophic respiration is smaller, the latter due to drier conditions.

1 Introduction

Terrestrial ecosystems on land take up about 3.3 Gt carbon per year on average (Friedlingstein et al., 2023). In order to estimate the magnitude of the land carbon sinks, dynamic global vegetation models are widely used. These models represent the terrestrial carbon cycle processes with varying levels of complexity. Generally, they can be used in an offline mode driven by prescribed atmospheric forcing or in a fully interactive configuration within Earth System Models.

However, estimates of carbon fluxes are subject to substantial uncertainties. Previous studies have identified both the representation of terrestrial and biosphere processes (model uncertainty), and the atmospheric forcing as major sources of uncertainty. For example, Jung et al. (2007b) found that changes in model resolution or land-cover maps had little effect on the simulated gross primary productivity, but changes in either the terrestrial biosphere model or the atmospheric forcing significantly affected the results. In their study, uncertainties in atmospheric forcing are especially projected on interannual variations in gross primary productivity. Similarly, Hardouin et al. (2022) concluded that atmospheric forcing accounts for a large fraction of uncertainty in the variability of gross primary productivity (75%) and autotrophic respiration (90%), while playing a smaller role for heterotrophic respiration (30%). In addition, Ahlström et al. (2017) further demonstrated that biases

https://doi.org/10.5194/egusphere-2026-1493
Preprint. Discussion started: 8 April 2026

in simulated precipitation, temperature, and downward shortwave radiation can explain up to 40% of the spread in land carbon fluxes and carbon pools estimates among Earth System models. Schaphoff et al. (2006) found that, under future projections, large variations in simulated precipitation patterns can even change the signs of land carbon uptake in tropical and sub-tropical ecosystems.

Global carbon estimates under present and future climates have relied on global datasets derived from Earth System models, which are typically run at coarse resolution, on the order of 100 km (e.g. Qian et al., 2010; Ahlström et al., 2017; Schaphoff et al., 2006; Morales et al., 2007; Müller et al., 2007; Fisher et al., 2022). Even regional estimates have often used coarse atmospheric forcing data, at best around 25 km (Jung et al., 2007a; Vetter et al., 2008; Huntzinger et al., 2013). At such grid spacings, convective processes – one of the two main mechanisms producing precipitation – must be parameterized. Convective parameterizations are known to introduce various biases in the representation of precipitation (e.g. Fiedler et al., 2020). One well-known bias is the overestimation of the frequency of light precipitation events and corresponding underestimation of intense events, commonly referred to as the "drizzle" problem (e.g Sun et al., 2005; Dai, 2006; Lazoglou et al., 2024). Refining the grid spacing to a few kilometers, typically below about 10 km, allows deep convective parameterizations to be switched off and deep convection to be explicitly resolved by the underlying fluid-dynamical equations. Comparisons between km-scale models and coarse-resolution climate models with convective parameterization have consistently shown a reduction of the drizzle problem (e.g. Prein et al., 2015; Schär et al., 2020; Stevens et al., 2020). Instead of drizzling, km-scale models with explicit convection produce more intense and shorter-lived daily precipitation events, in better agreement with observations.

Here, we propose the hypothesis that explicitly resolved convection enhances gross primary productivity. The underlying idea is that shorter-lived precipitation events allow more radiation to reach the surface on rainy days, thereby increasing photosynthesis and gross primary productivity. To test this hypothesis, we conduct two offline simulations using the terrestrial biosphere model JSBACH (Jena Scheme for Biosphere Atmosphere Coupling in Hamburg) (Schneck et al., 2022). One simulation is performed at a grid spacing of 5 km using atmospheric forcing derived from a 5-km global climate simulation with explicit convection, while the other simulation is conducted at a grid spacing of 160 km with atmospheric forcing taken from a coarse-resolution climate (160 km) model with parameterized convection. To reduce computational costs, particularly those associated with spinning up the carbon pools, we confine our study domain to Europe.

The atmospheric forcing used to drive the JSBACH simulation is derived from two distinct global climate models, with their own set of parameterizations and setups. In that sense, the two climate simulations differ in more aspects than only their representation of convection. In particular, Lee and Hohenegger (2024) showed that the strength and sign of the soil moisture-precipitation feedback in a global km-scale coupled climate simulation differ from those in a coarse-resolution global coupled climate simulation. Moreover, the two simulations exhibit different climatologies in terms of the amount and spatial distribution of precipitation, as well as radiation and temperature, which will affect the carbon fluxes simulated by JSBACH. Higher resolution also comes with a better representation of orography and land surface properties. Yet, we retain all these differences as we also want to see whether the potential effect of precipitation duration on carbon fluxes is sufficiently strong and systematic to influence the overall carbon fluxes despite the other differences.

https://doi.org/10.5194/egusphere-2026-1493
Preprint. Discussion started: 8 April 2026

The outline of the paper is as follows: Section 2 describes the JSBACH model and the design of the two experiments. Section 3 first quantifies the carbon fluxes and their differences in the two simulations, focusing on gross primary productivity, autotrophic respiration, heterotrophic respiration and grazing by herbivores. It then explains for each carbon flux the mechanisms underlying the differences found between the two simulations, especially testing the previously mentioned hypothesis. Section 4 summarizes the results.

2 Model description

2.1 JSBACH

JSBACH version 4 (Schneck et al., 2022) is the land component of the ICON Earth System model and its previous version was the land component of ICON's predecessor, the MPI Earth System model (Mauritsen et al., 2019). JSBACH represents both the physical and the biogeophysical processes of the land surface. Soil temperature is computed by solving the thermal diffusion equation, discretized over a finite number of soil layers. Soil moisture is predicted by the one-dimensional Richards equation. For the biogeophysical processes, we only consider the carbon cycle without any disturbance (e.g., fire). The core of the carbon module consists of assimilation of carbon through photosynthesis and the loss of water and carbon through plants transpiration. These processes are parameterized using components of the BETHY model (Knorr, 1997, 2000). The photosynthesis module first computes potential productivity under the assumption of unlimited water availability. Using unstressed stomatal conductance, the potential water loss through transpiration is calculated, from which the water-stressed stomatal conductance is derived. With this actual stomatal conductance, the model then computes the actual productivity per leaf area. The photosynthesis module accounts for physiological differences between plants by using the Farquhar model for C3 plants (Farquhar et al., 1980) and the Collatz model (Collatz et al., 1992) for C4 plants. Gross primary productivity is obtained by multiplying productivity per leaf area by the leaf area index, which is simulated using the phenology model LoGro-P (Logistic Growth Phenology). Net primary productivity is determined by subtracting autotrophic respiration from gross primary productivity. Net primary productivity is then allocated to three carbon pools: the wood pool (stems, branches, and roots), the green pool (leaves, fine roots, and vascular tissues), and the reserve pool (sugars and starches). The green pool looses carbon to the atmosphere through grazing by herbivores. The three carbon pools loose carbon to the soil through litterfall processes such as shedding of leaves, sapwood and littering. The soil carbon module consists of woody and non-woody litter, which can occur above or below ground. The dynamics of litter and soil carbon are parameterized using the Yasso07 model (Liski et al., 2005; Tuomi et al., 2009). Carbon is returned from the soil to the atmosphere via heterotrophic respiration. Hence, in equilibrium, carbon uptake through gross primary productivity is balanced by carbon losses through autotrophic respiration, heterotrophic respiration and grazing by herbivores.

https://doi.org/10.5194/egusphere-2026-1493
Preprint. Discussion started: 8 April 2026

2.2 Experimental design

We conduct two offline simulations with the JSBACH model, integrated at two distinct grid spacings with corresponding distinct atmospheric forcings. The first simulation is performed at a grid spacing of 5 km, using atmospheric forcing derived from a global storm-resolving model simulation conducted with the Sapphire configuration of the ICON model (Hohenegger et al., 2023) at the same grid spacing of 5 km. The set-up of the ICON simulation is described in Segura et al. (2025), where it is referred to as ICON-C3. The atmospheric forcing is available every 3 hours for four years. The first year of the five-year ICON-C3 simulation is excluded as spin-up. The second offline JSBACH simulation is integrated at a grid spacing of 160 km and uses atmospheric forcing derived from the MPI-ESM1.2-LR.piControl (Wieners et al., 2019) simulation, also available at a grid spacing of 160 km. The atmospheric forcing is available every 6 hours and we selected four years (1864-1867) for consistency with the first experiment. In the following, we refer to the first JSBACH simulation as SRM (for storm-resolving model) and the second one as LR (for low resolution). The main difference between the two atmospheric forcings is that the 5-km simulation (i.e., ICON-C3) only parameterizes radiation, microphysics and turbulence, whereas the 160-km simulation (i.e., MPI-ESM1.2-LR.piControl) employs the full suite of parameterizations, including a convection scheme. Note that both ICON-C3 and MPI-ESM1.2-LR.piControl use JSBACH as their land surface model in its light version. The atmospheric forcing variables needed to derive JSBACH are surface precipitation, downward shortwave and longwave radiation, as well as the near-surface (lowest atmospheric layer) humidity, temperature and wind speed. In both simulations, we fix the atmospheric CO_2 concentration to 367 ppmv throughout the simulation to simplify the analysis. Therefore, the carbon budget between the terrestrial ecosystem and the atmosphere is closed.

The two simulations cover Europe (Fig. 1a and b). To estimate carbon fluxes, JSBACH needs land parameter maps, such as albedo, soil type and plant functional type. These land parameter maps are derived from corresponding high-resolution observational datasets, with grid spacings of O(1 km) or finer and these maps are coarsened to the targeted grid spacings of 5 km and 160 km. For plant functional type, we use the ESA CCI land cover map (Store, 2019), which provides land cover type at a grid spacing of 300 m. We convert these land cover types to the plant functional types expected by JSBACH using a cross-walking table. In both simulations, we consider 11 plant functional types.

Both the SRM and LR simulations start from zero carbon fluxes and carbon pools. Thus, it is necessary to spin up the simulations over many years to reach equilibrium values. The humus pools require the longest time to spin up because they are associated with the slowest turnover processes. To accelerate the spin-up, JSBACH provides a special workflow that analytically estimates the equilibrium value of the humus pools based on their transient behavior. The humus pool values are then replaced by this analytically predicted equilibrium value. In the SRM and LR simulations, this workflow is applied once the difference in carbon flux into the humus pools between two consecutive years becomes smaller than 0.001 g C m^{-2} at every grid cell. After this step, the spin-up continues until the absolute difference in total ecosystem carbon between consecutive years is less than 1 g C m^{-2} at every grid cell, following McGuire et al. (1992) and Hoffman et al. (2014). The total spin-up time amounts to 556 years for the SRM simulation and 456 years for the LR simulation. After the carbon pools reach equilibrium, the simulations are continued for an additional four years, and the mean over these four years is used for analysis.

3 Result

3.1 Quantification of carbon flux differences

Figure 1 shows the four components of the carbon budget over the simulation domain (Europe), averaged over time, for LR, SRM, and their difference (SRM minus LR). The four components are: Gross Primary Productivity (GPP), autotrophic Respiration (Ra), heterotrophic Respiration (Rh) and grazing by herbivores. Because the simulations are in equilibrium, GPP is on average balanced by respiration and grazing and net ecosystem productivity is zero. Figure 1 reveals that the carbon fluxes are larger in SRM than in LR, except over central eastern Europe (Belarus, Ukraine, Romania, Serbia, Hungary, Slovakia, Czech Republic, Poland, and Turkey). The differences are largest for GPP and smallest for the carbon loss associated with grazing. Nevertheless, all four carbon fluxes exhibit a similar spatial difference pattern, with the negative differences over central eastern Europe and positive differences elsewhere. This difference pattern mostly reflects the spatial pattern of the carbon fluxes in SRM. Whereas the carbon fluxes in LR show very little zonal variations, there is a clear east-west contrast in SRM with smaller values over central eastern Europe.

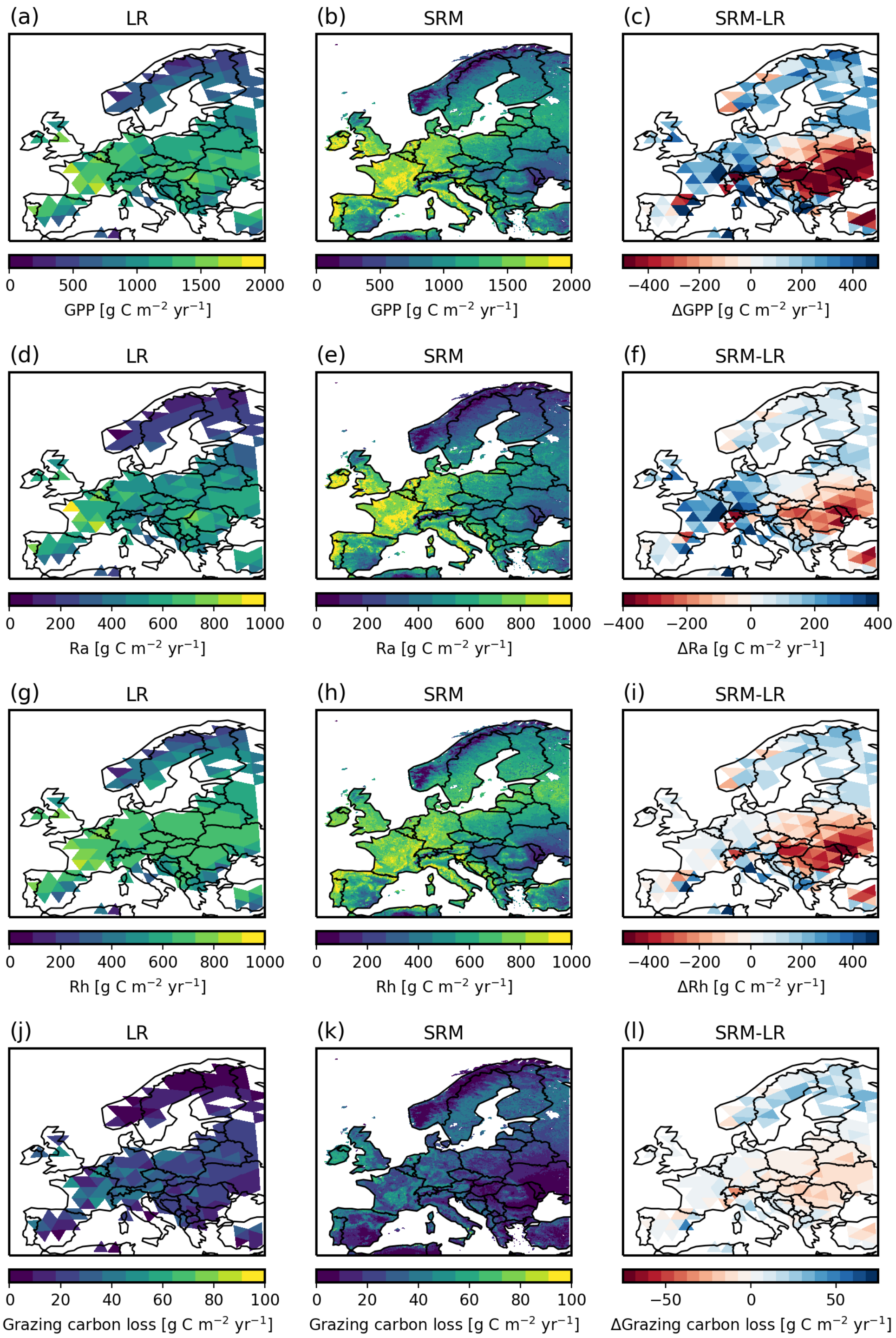

Figure 1. Carbon fluxes averaged over the four simulated years with (a-c) gross primary productivity (GPP), (d-f) autotrophic respiration (Ra), (g-i) heterotrophic respiration (Rh), and (j-l) carbon loss by grazing of herbivores for (left) LR, (center) SRM, and (right) the resulting difference (SRM-LR).

https://doi.org/10.5194/egusphere-2026-1493
Preprint. Discussion started: 8 April 2026

In addition, SRM shows much finer spatial structure in the simulated carbon fluxes than LR (Fig. 1). This difference is expected, as small-scale surface spatial variability is well resolved in the SRM, especially along the Alps, Carpathian, Pyrenees and Scandinavian mountains with the underlying high-resolution topography and land cover type.

To quantify the overall magnitude of the differences in carbon fluxes between the two simulations, we compute the mean carbon fluxes averaged over the land area of the simulation domain (Table 1). On average, SRM exhibits larger carbon uptake than LR. GPP is 1112.5 g C m^{-2} yr^{-1} in SRM, which is 22.3 g C m^{-2} yr^{-1} more than in LR. To balance this larger carbon uptake, SRM releases more carbon to the atmosphere. This happens primarily through higher Ra, which reaches 519.2 g C m^{-2} yr^{-1} in SRM, exceeding the LR value by 39.8 g C m^{-2} yr^{-1}. In contrast, Rh releases less carbon into the atmosphere in the SRM simulation (569.0 g C m^{-2} yr^{-1}) than in the LR simulation (588.0 g C m^{-2} yr^{-1}). The difference in carbon released through grazing by herbivores is small.

Table 1. Gross primary productivity (GPP), autotrophic respiration (Ra), heterotrophic respiration (Rh) and carbon loss by grazing of herbivores as averaged over Europe (land area of the domain) and the four simulated years (in g C m^{-2} yr^{-1}).

Variables	LR	SRM	Difference (SRM-LR)
GPP	1090.2	1112.5	22.3
Ra	479.4	519.2	39.8
Rh	588.0	569.0	-19.0
Grazing	22.8	24.2	1.4

To put these numbers into context, estimates of GPP generally show larger values over western central Europe than over eastern Europe and the Iberian Peninsula (e.g., Zhu et al., 2025; Pu et al., 2025; Yuan et al., 2025; Kang et al., 2025; Chen et al., 2024). Although uncertainties in GPP retrievals are large and different datasets do not always agree, values over western central Europe are typically around 1500-2000 g C m^{-2} yr^{-1}. The observed spatial pattern and averaged values are qualitatively consistent with the results shown in Fig. 1a,b. For Ra, the simulated values shown in Fig.1d,e also broadly agree with observation estimates, which typically range between 1000-1500 g C m^{-2} yr^{-1} over western central Europe (Ai et al., 2018; Zhu et al., 2025; Yuan et al., 2025). Regarding heterotrophic respiration, the dataset presented in Tang et al. (2020) has values of around 400-600 g C m^{-2} yr^{-1} in humid temperate areas over western and central Europe. These values are lower than those reported by Hashimoto et al. (2015), which range between 750-1000 g C m^{-2} yr^{-1} over western central Europe. The JSBACH simulations shown in Fig. 1g,h are thus in better agreement with the estimate reported by Hashimoto et al. (2015). The domain-mean GPP for Fluxnet2015 tower measurements (Pastorello et al., 2020) is 1480.6 ± 523.3 g C m^{-2} yr^{-1} (standard deviation across towers). In comparison, the gridded MODIS/Terra (Running and Zhao, 2021) yields a lower domain-mean of 1123.6 g C m^{-2} yr^{-1}. While the Multi-scale Synthesis and Terrestrial Model Intercomparison Project (MsTMIP) simulations (Huntzinger et al., 2018) show 899.9 ± 190.8 g C m^{-2} yr^{-1} (standard deviation across model members). In MsTMIP, Ra and Rh are estimated at 475.7 ± 154.8 and 447.1 ± 171.9 g C m^{-2} yr^{-1}, respectively. Overall, the JSBACH simulations (Table 1) reproduce the reported carbon flux magnitudes reasonably well.

3.2 What causes the differences in carbon fluxes?

3.2.1 Gross primary productivity

To first order, photosynthesis is mainly controlled by the amount of solar radiation, temperature and water availability (soil moisture) (Nemani et al., 2003; Beer et al., 2010). This is also the case in JSBACH, where GPP is modeled as a function of leaf area index and water-stressed plant productivity. For vegetation across Europe, leaf area index is mainly controlled by temperature and soil moisture, whereas plant productivity depends in particular on solar radiation and soil moisture. Table 2 shows the results of a multiple linear regression of GPP against surface downward shortwave radiation, 2-m air temperature, and root-zone soil moisture. In both SRM and LR, downward shortwave radiation plays the dominant role among the three factors. In both simulations, the regression coefficient for downward shortwave radiation is larger than 0.53, whereas the other two regression coefficients are smaller than 0.23. Averaged over the land areas, SRM receives about 22 W m^{-2} more shortwave radiation than LR, which is consistent with the larger GPP.

Table 2. Coefficients from the multiple linear regression of GPP with respect to downward solar radiation (SW), air temperature ($\mathrm{T_a}$) and root-zone soil moisture (SM), $\mathrm{GPP} = \beta_0 + \beta_{\mathrm{SW}} \cdot \mathrm{SW} + \beta_{\mathrm{T_a}} \cdot \mathrm{T_a} + \beta_{\mathrm{SM}} \cdot \mathrm{SM}$. Each dependent and independent variable is standardized to have zero mean and unit variance. Daily values at every grid point are used to compute the multiple linear regression.

Simulations	β_0	β_{SW}	$\beta_{\mathrm{T_a}}$	β_{SM}
LR	0	**0.53**	0.23	0.16
SRM	0	**0.57**	0.10	0.21

The differences in radiation may arise from the use of different radiation schemes between the two atmospheric forcing datasets and/or from the simulation of a different cloud cover. The latter would be supporting the hypothesis mentioned in the introduction, namely that the shift in the convective precipitation distribution – from long-lived drizzling rainfall in models with convective parameterizations to short-lived storms in models with explicit convection – could allow more solar radiation to reach the plants and thereby higher GPP. To further investigate this mechanism, we examine in more detail the relationships between GPP, precipitation, radiation, and precipitation duration (see Fig. 2).

Figure 2a reveals similar GPP in both simulations for precipitation amounts smaller than 10 mm day^{-1}, but much larger GPP in SRM for precipitation amounts larger than 10 mm day^{-1}. This behavior is consistent with the relationship between precipitation and downward shortwave radiation (Fig. 2b). In LR, radiation starts to decrease rapidly beyond 9 mm day^{-1} of precipitation, while it stays approximately constant with increasing precipitation in SRM. The fact that SRM can maintain high solar radiation despite strong precipitation could be due to shorter-lived precipitation events, as confirmed by Fig. 2c. Although SRM has slightly more rainfall events lasting 6 h and 12 h, it has substantially fewer full-day rainy days than LR. Rain occuring throughout the entire day accounts for only 17.6% in SRM, compared to 45.2% in LR.

To quantify the impact of these strong precipitation events on the overall mean GPP, we decompose the mean GPP into contributions from days with less than and greater than 10 mm day^{-1} of precipitation:

https://doi.org/10.5194/egusphere-2026-1493
Preprint. Discussion started: 8 April 2026

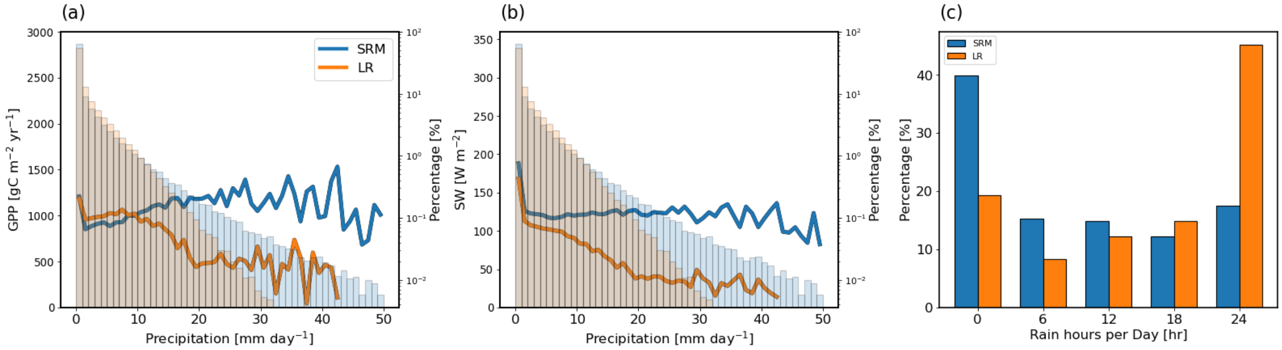

Figure 2. (a) Daily mean GPP as a function of daily mean precipitation for the LR (orange line) and the SRM (blue line) simulation and histogram of precipitation (bar). (b) Same as (a) but for surface downward shortwave radiation. (c) Histogram of rain hours per day in the two simulations.

$$\overline{\mathrm{GPP}} = \alpha \cdot \overline{\mathrm{GPP}_{\mathrm{P}<10}} + (1-\alpha) \cdot \overline{\mathrm{GPP}_{\mathrm{P}\geq 10}}, \tag{1}$$

where the overbar denotes averaging, P is precipitation and α is the fraction of events with $\mathrm{P} < 10$ mm day^{-1}. The values of each term are summarized in Table 3.

Table 3. Decomposition of land mean GPP (g C m^{-2} yr^{-1}) based on a daily mean precipitation threshold of 10 mm day^{-1} (see Eq. 1.)

Simulation	$\overline{\mathrm{GPP}}$	$\alpha \cdot \overline{\mathrm{GPP}_{\mathrm{P}<10}}$	$(1-\alpha) \cdot \overline{\mathrm{GPP}_{\mathrm{P}\geq 10}}$	α	$\overline{\mathrm{GPP}_{\mathrm{P}<10}}$	$\overline{\mathrm{GPP}_{\mathrm{P}\geq 10}}$
LR	1090.2	1055.8	34.4	0.96	1101.0	838.1
SRM	1112.5	1043.4	69.1	0.94	1112.0	1120.7
SRM-LR	22.3	-12.4	34.7	-0.02	11.0	282.7

Table 3 shows that the contribution is larger in SRM than in LR for the strong precipitation events ($(1-\alpha) \cdot \overline{\mathrm{GPP}_{\mathrm{P}\geq 10}}$), whereas it is slightly smaller for weak precipitation events ($\alpha \cdot \overline{\mathrm{GPP}_{\mathrm{P}<10}}$). Hence, the larger GPP on strongly precipitating days explains the larger mean GPP in SRM. The larger contribution of strong precipitation days to GPP, $(1-\alpha) \cdot \overline{\mathrm{GPP}_{\mathrm{P}\geq 10}}$, arises both from the larger conditional average of GPP, $\overline{\mathrm{GPP}_{\mathrm{P}\geq 10}}$, consistent with Fig. 2b, and from the more frequent occurrence of strong precipitation events, which is expected when convection is explicitly resolved.

Examined on a monthly basis, daily precipitation larger than 10 mm day^{-1} occurs throughout the year, with the largest differences in occurrence between the two simulations found in April, May, and June. This timing pinpoints to the importance of moist convection in generating these differences. Similarly, downward surface shortwave radiation is larger in SRM than in LR in every month. But the differences in downward surface shortwave radiation are consistently larger for the strongly precipitating events in April-June. For instance, in June, the differences are 47 W m^{-2} for the strong precipitation events, compared with 25 W m^{-2} for events with P$<$ 10 mm day^{-1}. Taken together, these results confirm the hypothesis that shorter-

https://doi.org/10.5194/egusphere-2026-1493
Preprint. Discussion started: 8 April 2026

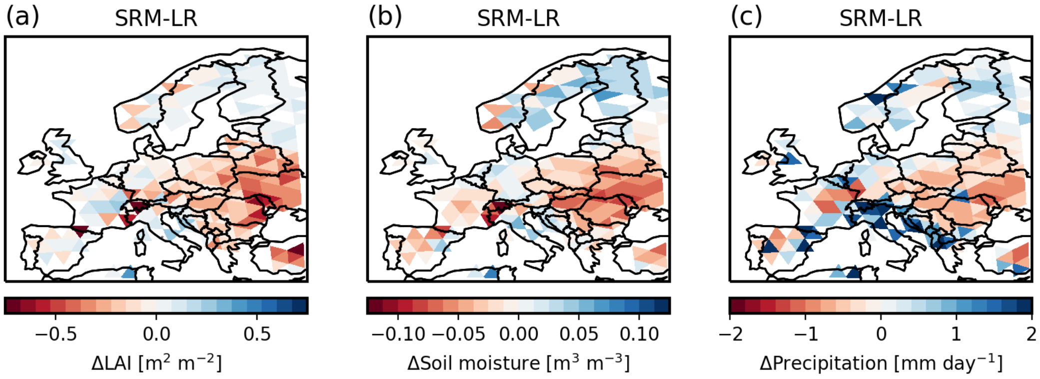

Figure 3. Maps of difference in (a) leaf area index (m^2 m^{-2}), (b) soil moisture (1st soil layer) (m^3 m^{-3}) and (c) precipitation (mm day^{-1}) between SRM and LR averaged over the four simulated years.

lived convective events due to the explicit representation of convection in SRM allow more solar radiation to reach the surface, thereby enhancing photosynthesis and ultimately increasing GPP.

There is, however, a subtlety. From the previous argument, one might expect larger GPP across the whole of Europe. Yet, central eastern Europe (Fig. 1) exhibits lower GPP. To understand this discrepancy, the difference maps between the SRM and LR simulations for leaf area index, soil moisture in the first soil layer, and precipitation are analyzed (Fig. 3). The time-averaged difference pattern in the leaf area index (Fig. 3a) resembles that of GPP in Fig. 1c, particularly the negative values over central eastern Europe. These negative values first appear in June near the northern boundary of the Black Sea and expand across the whole of central eastern Europe from July to September. The dominant plant functional types in this region are crop and grass, and they are also the two plant functional types whose associated leaf area index exhibit the typical east-west difference pattern over central Europe, with negative values in the East and positive values in the West. Both crop and grass require sufficient soil moisture to grow once the temperature becomes warm enough. As shown in Fig. 3b, soil moisture is substantially lower in SRM than in LR over eastern central Europe. First values of soil moisture below the critical threshold for plant growth appear in May near the northern border of the Black Sea. The lack of soil moisture over central eastern Europe correlates very well with a lack of precipitation (compare Fig. 3b and c). All in all, the difference patterns in precipitation, soil moisture, leaf area index and GPP are all consistent with each other. The reduced precipitation over central eastern Europe therefore explains the lower GPP in SRM compared to LR over that region. The importance of precipitation and soil moisture for GPP has been documented in past studies (e.g. Beer et al., 2010; Humphrey et al., 2021).

These findings are consistent with the result of the multiple linear regression shown in Table 2, where soil moisture appears to play an important role for GPP in SRM. Hence, perhaps not surprisingly, the different climatologies between SRM and LR, especially in terms of mean precipitation, modulate the expected increase in GPP associated with explicit convection and shorter-lived convective events. In our case, however, the latter effect still wins on average.

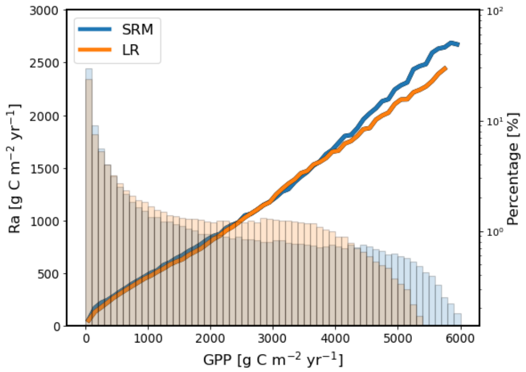

Figure 4. Daily mean values of Ra as a function of daily mean values of GPP for the LR (orange line) and the SRM (blue line) simulations with histogram of GPP (bar).

3.2.2 Autotrophic respiration

In JSBACH, Ra consists of dark respiration (maintenance respiration) and growth respiration. Dark respiration per leaf area is a function of air temperature and downward shortwave radiation, following the Farquhar and Collatz models of photosynthesis, whereas growth respiration is proportional to GPP. Table 4 shows the result of the multiple linear regression between Ra and its controlling factors, namely GPP, $\mathrm{T_a}$ and SW. It is clear from Table 4 that GPP is the dominant controlling factor as its regression coefficient is larger than 0.86. Further examining the relationship between GPP and Ra using Fig. 4, we see that Ra indeed increases linearly with GPP in both simulations over the range of simulated GPP values. The functional relationship is identical in both simulations up to a GPP value of about 4000 g C $\mathrm{m^{-2}}$ $\mathrm{yr^{-1}}$. Because SRM produces more extreme GPP values (see histogram on Fig. 4) and simulates a larger mean GPP, Ra is also larger on average in SRM than in LR. The mean value is 479.4 g C $\mathrm{m^{-2}}$ $\mathrm{yr^{-1}}$ in SRM, which is 39.9 g C $\mathrm{m^{-2}}$ $\mathrm{yr^{-1}}$ larger than in LR.

Table 4. Same as Table 2 but from the multiple linear regression of Ra with respect to GPP, $\mathrm{T_a}$ and SW, $\mathrm{Ra} = \beta_0 + \beta_{\mathrm{GPP}} \cdot \mathrm{GPP} + \beta_{\mathrm{T_a}} \cdot \mathrm{T_a} + \beta_{\mathrm{SW}} \cdot \mathrm{SW}$.

Simulations	β_0	β_{GPP}	$\beta_{\mathrm{T_a}}$	β_{SW}
LR	0	**0.91**	0.14	-0.088
SRM	0	**0.86**	0.20	-0.088

3.2.3 Heterotrophic respiration

Rh is modelled using the Yasso07 scheme (Liski et al., 2005; Tuomi et al., 2009). It is proportional to a climate-dependent function, k_{clim} parameter, given as,

$$k_{\mathrm{clim}} = e^{\beta_1 \overline{\mathrm{T_c}} + \beta_2 \overline{\mathrm{T_c}}^2}(1 - e^{\gamma \overline{\mathrm{P_m}}}), \tag{2}$$

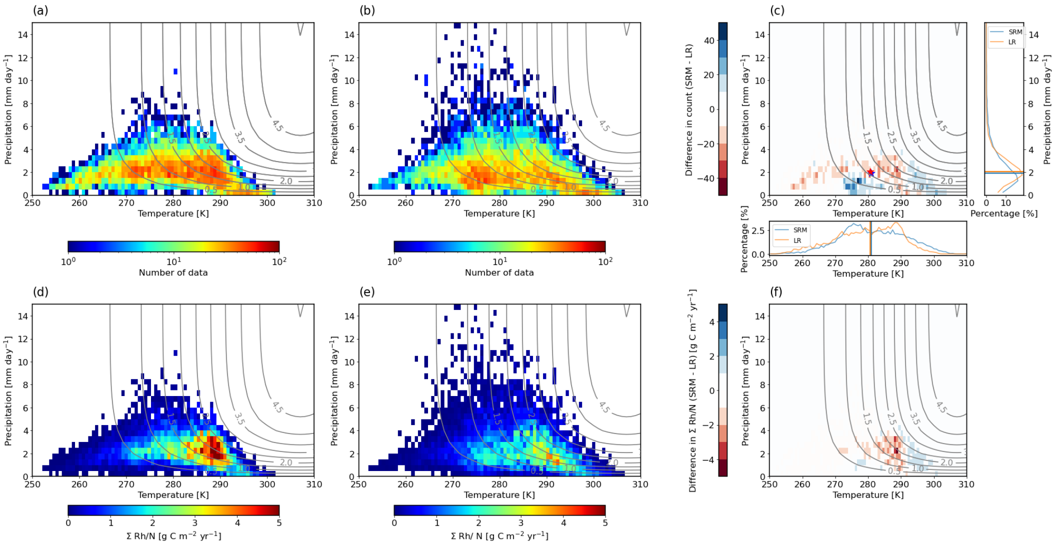

Figure 5. (a, b) Two-dimensional histogram (shading) of monthly mean air temperature and precipitation in (a) the LR simulation, (b) the SRM simulation and (c) their difference (SRM-LR). In panel c, the two insets are for the histogram of precipitation (right) and of temperature (bottom). Stars indicate medians of monthly mean air temperature and precipitation in the LR simulation (red star) and in the SRM simulation (blue star). The lower row (d-f) shows the contribution of each bin to the mean of Rh, which is computed as the sum of Rh within each bin divided by the total number of data for (d) the LR simulation, (e) the SRM simulation and (f) their difference, see text for more detail. Grey contour lines represent the analytic solution of k_{clim}, see Eq. 2.

where $\overline{\mathrm{T_c}}$ is the 30-day mean air temperature in °C and $\overline{\mathrm{P_m}}$ is the 30-day mean precipitation in m yr^{-1}. The parameters β_1=0.095 $°\mathrm{C}^{-1}$, β_2=-0.0014 $°\mathrm{C}^{-2}$, and γ=-1.21 yr m^{-1} are fitted parameters. The k_{clim} plays an equivalent role to the Q10 parameter in other soil carbon models. Accordingly, Rh is a function of monthly mean air temperature ($\overline{\mathrm{T_a}}$) and precipitation ($\overline{\mathrm{P}}$).

We first examine the analytic solution of k_{clim} with Eq. (2) to understand the influence of $\overline{\mathrm{T_a}}$ and $\overline{\mathrm{P}}$ on k_{clim} (see the grey contour lines in Fig. 5). When $\overline{\mathrm{P}}$ <4 mm day^{-1}, k_{clim} increases with both temperature and precipitation, reflecting the fact that decomposition becomes more active under moist and warm conditions. When $\overline{\mathrm{P}} \geq$ 4 mm day^{-1}, k_{clim} becomes largely insensitive to further increases in precipitation and instead increases mainly with temperature. This weak sensitivity to precipitation suggests that moisture is no longer a limiting factor for decomposition, because moisture is already large enough in $\overline{\mathrm{P}}$ ≥4 mm day^{-1} conditions.

Using the insight from the analytic solution of k_{clim}, we investigate why Rh is smaller in SRM (569.0 g C m^{-2} yr^{-1}) than in LR (588.0 g C m^{-2} yr^{-1}). Looking at Fig. 5a and b, we see that most data points in both simulations occur under $\overline{\mathrm{P}}$ <4 mm day^{-1} condition (≥90%), where both precipitation and temperature influence k_{clim}. A visual comparison of these two panels suggests that SRM contains more data points at smaller monthly mean precipitation amounts than LR. This is confirmed by Fig. 5c, especially in the precipitation histogram on the right. SRM has more data points than LR when $\overline{\mathrm{P}}$ ≤1.5 mm day^{-1}, by

https://doi.org/10.5194/egusphere-2026-1493
Preprint. Discussion started: 8 April 2026

8%, corresponding to a frequency of occurrence of 37%. In contrast, LR has more data points when 1.5< $\overline{\mathrm{P}}$ ≤4 mm day^{-1}, by 14%, and its frequency of occurrence is 63%. A larger occurrence of smaller monthly mean precipitation amounts implies a smaller k_{clim}, which is consistent with the weaker Rh found in SRM compared to LR. Likewise, the median value of $\overline{\mathrm{P}}$ is smaller in SRM compared to LR, with a value of 1.9 versus 2.1 mm day^{-1}, respectively.

Looking now at the temperature dependency, SRM has more data points for 275< $\overline{\mathrm{T_a}}$ <280 K and $\overline{\mathrm{T_a}}$ >290 K, whereas LR has more data points for $\overline{\mathrm{T_a}}$ <270 and 280< $\overline{\mathrm{T_a}}$ <290 K (see particularly the temperature histogram in Fig. 5c). The medians of $\overline{\mathrm{T_a}}$ are 281.0 K in SRM and 280.6 K in LR, hence the median is warmer in SRM. This effect alone would suggest a higher k_{clim} and therefore higher Rh in SRM compared to LR, which is opposite to what is found. Hence, we conclude that the differences in precipitation between the two simulations are more important than the differences in temperature and explain the weaker Rh in SRM. Moreover, the median values of k_{clim} confirm this result. The medians are 1.10 in SRM and 1.12 in LR. If only $\overline{\mathrm{P}}$ decreases from the median LR value (2.1 mm day^{-1}) to the SRM value (1.9 mm day^{-1}), k_{clim} would decrease by 0.04. In contrast, if only $\overline{\mathrm{T_a}}$ increases from the median LR value (280.6 K) to the SRM one (281.0 K), k_{clim} would increase by 0.03. The effect of precipitation, therefore, dominates. This is also consistent with the findings of Tang et al. (2020), who used a random forest algorithm to derive a gridded Rh dataset based on field observations from the Global Soil Respiration Database and environmental drivers. According to their study, precipitation is the main driver for Rh for latitudes between 25° and 50°N, whereas temperature becomes the dominant driving factor north of 50°N. Using the dataset produced by Hashimoto et al. (2015), which was based on a semi-empirical model, they even found precipitation and soil moisture to be the dominant drivers across Europe.

The above interpretation relies on k_{clim} as a proxy for Rh rather than directly on the values of Rh. In Fig. 5d-f, we now plot the values of Rh as a function of $\overline{\mathrm{T_a}}$ and $\overline{\mathrm{P}}$. To do so, we first sum all the values of Rh within each bin ($\sum \mathrm{Rh}$) and then divide this sum by the total number of data points (N=8,736), yielding $\sum \mathrm{Rh}/N$ for each bin. If we sum $\sum \mathrm{Rh}/N$ over all bins, we get the value of Rh listed in Table 1. Figures 5d-f indeed show that LR contributes more strongly to Rh than SRM where the values of k_{clim} are also higher, for example around 290 K and 2 mm day^{-1}. Near $k_{\mathrm{clim}} = 2$, $\sum \mathrm{Rh}/N$ peaks in LR, with values exceeding 5 g C m^{-2} yr^{-1}. In contrast, SRM reaches values of only up to about 3.5 g C m^{-2} yr^{-1} in the same region. The more frequent wetter conditions therefore lead to stronger Rh in LR. In conclusion, Rh is smaller in SRM because i) SRM has more data points by weaker monthly mean precipitation and ii) precipitation is the main driving factor for Rh, even though SRM exhibits slightly warmer temperatures.

3.2.4 Grazing of herbivores

Carbon losses due to grazing of herbivores are similar in both simulations. The loss is slightly higher in SRM, with a value of 24.2 g C m^{-2} yr^{-1} compared to 22.8 g C m^{-2} yr^{-1} in LR. In JSBACH, grazing of herbivores is proportional to the amount of carbon available in the green pool, which represents the carbon stored in the living parts of plants, the "green" part. The green pool is larger in SRM than in LR by 66.6 g C m^{-2}. Although the difference between the two simulations is consistent with expectations, its overall magnitude is rather negligible.

https://doi.org/10.5194/egusphere-2026-1493
Preprint. Discussion started: 8 April 2026

4 Summary

In this study, we investigated the magnitude of the carbon fluxes over Europe in two offline simulations conducted with the land surface model JSBACH. One simulation is driven by atmospheric forcing from a coarse-resolution climate model simulation, referred to as LR, while the other simulation uses atmospheric forcing from a km-scale simulation, referred to as SRM. The coarse-resolution climate simulation had been performed with MPI-ESM1.2-LR.piControl at a grid spacing of 160 km, whereas the km-scale simulation had been performed with the Sapphire configuration of the ICON model at a grid spacing of 5 km. The key difference between the two climate simulations is that convection is parameterized at 160 km, but explicitly resolved at 5 km. The hypothesis motivating this study is that explicitly resolving convection at the km scale, rather than parameterizing it, leads to shorter and more intense daily precipitation events. Shorter precipitation events imply less longer-lasting cloud cover, hence more shortwave radiation to reach the surface, which can be used by plants for photosynthesis and may enhance gross primary productivity. The two offline simulations were set out to test this hypothesis.

Comparing the two simulations, we find that the land surface in SRM takes up more carbon. Gross primary productivity is 1112.5 g C m^{-2} yr^{-1} in SRM versus 1090.2 g C m^{-2} yr^{-1} in LR. Regarding carbon losses, autotrophic respiration is larger in SRM by 39.8 g C m^{-2} yr^{-1}, whereas heterotrophic respiration is smaller by 19.0 g C m^{-2} yr^{-1}. Differences in carbon losses due to grazing by herbivores are negligible.

To understand the causes of these differences in carbon fluxes, we explored the underlying main driving factors of the carbon fluxes. For gross primary productivity, the largest differences between the two simulations occur for daily precipitation amounts exceeding 10 mm day^{-1}. These events are also associated with larger downward shortwave radiation in SRM and appear to be shorter-lived. For instance, whole day events occur 18% of the time in SRM compared to 45% in LR. Hence, in agreement with our hypothesis, stronger precipitation events are shorter-lived in SRM, allowing more solar radiation to be absorbed by the plants and leading to a higher gross primary productivity. As autotrophic respiration is largely controlled by gross primary productivity, the larger productivity directly explains the larger autotrophic respiration found in SRM. Finally, regarding heterotrophic respiration, SRM is more often associated with warmer monthly mean conditions, which alone would increase heterotrophic respiration. At the same time, however, SRM is more often associated with drier conditions, characterized by weaker monthly mean precipitation. In comparison, LR has more data points with monthly mean precipitation between 1.5 and 4 mm day^{-1}. The functional dependency of heterotrophic respiration on precipitation implies that respiration increases with precipitation up to about 4 mm day^{-1} before reaching a plateau. Hence, the effect of precipitation on heterotrophic respiration wins over the temperature effect and explains the smaller heterotrophic respiration in SRM.

Besides these differences in mean quantities, we also find a specific spatial difference pattern. Carbon fluxes in SRM are typically larger over western central Europe and northern Europe, but smaller over eastern Europe compared to LR. This pattern reflects a more pronounced zonal gradient in carbon fluxes in SRM. The spatial differences are consistent with the difference pattern in precipitation and simulated soil moisture. Over eastern Europe, SRM exhibits weaker precipitation and, consequently, lower soil moisture than LR. Soil moisture becomes too low and the dominant plant functional types in this region (grass and crop) begin to wilt by the end of May. The anomaly first appears around the northern border of the Black Sea and gradually extends across eastern Europe over time. Hence, although explicitly resolving convection favors higher gross primary productivity through shorter-lived, intense daily precipitation events, the overall climatology modulates this effect. In our case, the deficit in precipitation in SRM over eastern Europe leads to reduced productivity in that region. However, when averaged over the entire simulation domain, the increase in productivity still dominates.

Author contributions. JL and CH designed research; performed research; analyzed the data; and drafted the paper.

Competing interests. The authors declare no competing interest.

Acknowledgements. The study was supported by the NextGEMS (Grant No. 101003470) and the Max Planck society for the advancement of science. Open access funding is provided by the Max Planck Society. We thank Seung Hee Seo for thorough discussions on the research and writing and Tamara Emmerichs for internally reviewing the manuscript, which helped strengthen and clarify our manuscript. The simulations were performed using the facilities of the DKRZ (Deutsches Klimarechenzentrum).

References

Ahlström, A., Schurgers, G., and Smith, B.: The large influence of climate model bias on terrestrial carbon cycle simulations, Environmental Research Letters, 12, 014 004, 2017.

Ai, J., Jia, G., Epstein, H. E., Wang, H., Zhang, A., and Hu, Y.: MODIS-Based Estimates of Global Terrestrial Ecosystem Respiration, Journal of Geophysical Research: Biogeosciences, 123, 326–352, https://doi.org/https://doi.org/10.1002/2017JG004107, 2018.

Beer, C., Reichstein, M., Tomelleri, E., Ciais, P., Jung, M., Carvalhais, N., Rödenbeck, C., Arain, M. A., Baldocchi, D., Bonan, G. B., Bondeau, A., Cescatti, A., Lasslop, G., Lindroth, A., Lomas, M., Luyssaert, S., Margolis, H., Oleson, K. W., Roupsard, O., Veenendaal, E., Viovy, N., Williams, C., Woodward, F. I., and Papale, D.: Terrestrial Gross Carbon Dioxide Uptake: Global Distribution and Covariation with Climate, Science, 329, 834–838, https://doi.org/10.1126/science.1184984, 2010.

Chen, X., Chen, T., Li, X., Chai, Y., Zhou, S., Guo, R., and Dai, J.: A 2001–2022 global gross primary productivity dataset using an ensemble model based on the random forest method, Biogeosciences, 21, 4285–4300, https://doi.org/10.5194/bg-21-4285-2024, 2024.

Collatz, G. J., Ribas-Carbo, M., and Berry, J. A.: Coupled photosynthesis-stomatal conductance model for leaves of C4 plants, Functional Plant Biology, 19, 519–538, 1992.

Dai, A.: Precipitation characteristics in eighteen coupled climate models, Journal of climate, 19, 4605–4630, 2006.

Farquhar, G. D., von Caemmerer, S. v., and Berry, J. A.: A biochemical model of photosynthetic CO 2 assimilation in leaves of C 3 species, planta, 149, 78–90, 1980.

Fiedler, S., Crueger, T., D'Agostino, R., Peters, K., Becker, T., Leutwyler, D., Paccini, L., Burdanowitz, J., Buehler, S. A., Cortes, A. U., Dauhut, T., Dommenget, D., Fraedrich, K., Jungandreas, L., Maher, N., Naumann, A. K., Rugenstein, M., Sakradzija, M., Schmidt, H., Sielmann, F., Stephan, C., Timmreck, C., Zhu, X., and Stevens, B.: Simulated Tropical Precipitation Assessed across Three Major Phases of the Coupled Model Intercomparison Project (CMIP), Monthly Weather Review, 148, 3653 – 3680, https://doi.org/10.1175/MWR-D-19-0404.1, 2020.

Fisher, J. B., Sikka, M., Block, G. L., Schwalm, C. R., Parazoo, N. C., Kolus, H. R., Sok, M., Wang, A., Gagne-Landmann, A., Lawal, S., et al.: The terrestrial biosphere model farm, Journal of advances in modeling earth systems, 14, e2021MS002 676, 2022.

Friedlingstein, P., O'Sullivan, M., Jones, M. W., Andrew, R. M., Bakker, D. C. E., Hauck, J., Landschützer, P., Le Quéré, C., Luijkx, I. T., Peters, G. P., Peters, W., Pongratz, J., Schwingshackl, C., Sitch, S., Canadell, J. G., Ciais, P., Jackson, R. B., Alin, S. R., Anthoni, P., Barbero, L., Bates, N. R., Becker, M., Bellouin, N., Decharme, B., Bopp, L., Brasika, I. B. M., Cadule, P., Chamberlain, M. A., Chandra, N., Chau, T.-T.-T., Chevallier, F., Chini, L. P., Cronin, M., Dou, X., Enyo, K., Evans, W., Falk, S., Feely, R. A., Feng, L., Ford, D. J., Gasser, T., Ghattas, J., Gkritzalis, T., Grassi, G., Gregor, L., Gruber, N., Gürses, O., Harris, I., Hefner, M., Heinke, J., Houghton, R. A., Hurtt, G. C., Iida, Y., Ilyina, T., Jacobson, A. R., Jain, A., Jarníková, T., Jersild, A., Jiang, F., Jin, Z., Joos, F., Kato, E., Keeling, R. F., Kennedy, D., Klein Goldewijk, K., Knauer, J., Korsbakken, J. I., Körtzinger, A., Lan, X., Lefèvre, N., Li, H., Liu, J., Liu, Z., Ma, L., Marland, G., Mayot, N., McGuire, P. C., McKinley, G. A., Meyer, G., Morgan, E. J., Munro, D. R., Nakaoka, S.-I., Niwa, Y., O'Brien, K. M., Olsen, A., Omar, A. M., Ono, T., Paulsen, M., Pierrot, D., Pocock, K., Poulter, B., Powis, C. M., Rehder, G., Resplandy, L., Robertson, E., Rödenbeck, C., Rosan, T. M., Schwinger, J., Séférian, R., Smallman, T. L., Smith, S. M., Sospedra-Alfonso, R., Sun, Q., Sutton, A. J., Sweeney, C., Takao, S., Tans, P. P., Tian, H., Tilbrook, B., Tsujino, H., Tubiello, F., van der Werf, G. R., van Ooijen, E., Wanninkhof, R., Watanabe, M., Wimart-Rousseau, C., Yang, D., Yang, X., Yuan, W., Yue, X., Zaehle, S., Zeng, J., and Zheng, B.: Global Carbon Budget 2023, Earth System Science Data, 15, 5301–5369, https://doi.org/10.5194/essd-15-5301-2023, 2023.

Hardouin, L., Delire, C., Decharme, B., Lawrence, D. M., Nabel, J. E., Brovkin, V., Collier, N., Fisher, R., Hoffman, F. M., Koven, C. D., et al.: Uncertainty in land carbon budget simulated by terrestrial biosphere models: the role of atmospheric forcing, Environmental Research Letters, 17, 094 033, 2022.

Hashimoto, S., Carvalhais, N., Ito, A., Migliavacca, M., Nishina, K., and Reichstein, M.: Global spatiotemporal distribution of soil respiration modeled using a global database, Biogeosciences, 12, 4121–4132, 2015.

Hoffman, F. M., Randerson, J. T., Arora, V. K., Bao, Q., Cadule, P., Ji, D., Jones, C. D., Kawamiya, M., Khatiwala, S., Lindsay, K., et al.: Causes and implications of persistent atmospheric carbon dioxide biases in Earth System Models, Journal of Geophysical Research: Biogeosciences, 119, 141–162, 2014.

Hohenegger, C., Korn, P., Linardakis, L., Redler, R., Schnur, R., Adamidis, P., Bao, J., Bastin, S., Behravesh, M., Bergemann, M., et al.: ICON-Sapphire: simulating the components of the Earth system and their interactions at kilometer and subkilometer scales, Geoscientific Model Development, 16, 779–811, 2023.

Humphrey, V., Berg, A., Ciais, P., Gentine, P., Jung, M., Reichstein, M., Seneviratne, S. I., and Frankenberg, C.: Soil moisture–atmosphere feedback dominates land carbon uptake variability, Nature, 592, 65–69, https://doi.org/10.1038/s41586-021-03325-5, 2021.

Huntzinger, D., Schwalm, C., Michalak, A., Schaefer, K., King, A., Wei, Y., Jacobson, A., Liu, S., Cook, R., Post, W., et al.: The North American carbon program multi-scale synthesis and terrestrial model intercomparison project–Part 1: Overview and experimental design, Geoscientific Model Development, 6, 2121–2133, 2013.

Huntzinger, D., Schwalm, C., Wei, Y., Cook, R., Michalak, A., Schaefer, K., Jacobson, A., Arain, M., Ciais, P., Fisher, J., et al.: NACP MsTMIP: Global 0.5-degree Model Outputs in Standard Format, Version 1.0. ORNL DAAC, Oak Ridge, Tennessee, USA, 2018.

Jung, M., Le Maire, G., Zaehle, S., Luyssaert, S., Vetter, M., Churkina, G., Ciais, P., Viovy, N., and Reichstein, M.: Assessing the ability of three land ecosystem models to simulate gross carbon uptake of forests from boreal to Mediterranean climate in Europe, Biogeosciences, 4, 647–656, 2007a.

Jung, M., Vetter, M., Herold, M., Churkina, G., Reichstein, M., Zaehle, S., Ciais, P., Viovy, N., Bondeau, A., Chen, Y., et al.: Uncertainties of modeling gross primary productivity over Europe: A systematic study on the effects of using different drivers and terrestrial biosphere models, Global Biogeochemical Cycles, 21, 2007b.

Kang, Y., Bassiouni, M., Gaber, M., Lu, X., and Keenan, T. F.: CEDAR-GPP: spatiotemporally upscaled estimates of gross primary productivity incorporating CO_2 fertilization, Earth System Science Data, 17, 3009–3046, https://doi.org/10.5194/essd-17-3009-2025, 2025.

Knorr, W.: Satellite remote sensing and modelling of the global CO2 exchange of land vegetation: a synthesis study, Max-Planck-Institut fur Meteorologie Examensarbeit, 49, 185, 1997.

Knorr, W.: Annual and interannual CO2 exchanges of the terrestrial biosphere: Process-based simulations and uncertainties, Global ecology and biogeography, 9, 225–252, 2000.

Lazoglou, G., Economou, T., Anagnostopoulou, C., Zittis, G., Tzyrkalli, A., Georgiades, P., and Lelieveld, J.: Multivariate adjustment of drizzle bias using machine learning in European climate projections, Geoscientific Model Development, 17, 4689–4703, https://doi.org/10.5194/gmd-17-4689-2024, 2024.

Lee, J. and Hohenegger, C.: Weaker land–atmosphere coupling in global storm-resolving simulation, Proceedings of the National Academy of Sciences, 121, e2314265 121, 2024.

Liski, J., Palosuo, T., Peltoniemi, M., and Sievanen, R.: Carbon and decomposition model Yasso for forest soils, Ecological Modelling, pp. 168–182, 2005.

Mauritsen, T., Bader, J., Becker, T., Behrens, J., Bittner, M., Brokopf, R., Brovkin, V., Claussen, M., Crueger, T., Esch, M., et al.: Developments in the MPI-M Earth System Model version 1.2 (MPI-ESM1. 2) and its response to increasing CO2, Journal of Advances in Modeling Earth Systems, 11, 998–1038, 2019.

McGuire, A. D., Melillo, J. M., Joyce, L., Kicklighter, D. W., Grace, A., Moore III, B., and Vorosmarty, C. J.: Interactions between carbon and nitrogen dynamics in estimating net primary productivity for potential vegetation in North America, Global Biogeochemical Cycles, 6, 101–124, 1992.

Morales, P., Hickler, T., Rowell, D. P., Smith, B., and Sykes, M. T.: Changes in European ecosystem productivity and carbon balance driven by regional climate model output, Global Change Biology, 13, 108–122, 2007.

Müller, C., Eickhout, B., Zaehle, S., Bondeau, A., Cramer, W., and Lucht, W.: Effects of changes in CO2, climate, and land use on the carbon balance of the land biosphere during the 21st century, Journal of Geophysical Research: Biogeosciences, 112, 2007.

Nemani, R. R., Keeling, C. D., Hashimoto, H., Jolly, W. M., Piper, S. C., Tucker, C. J., Myneni, R. B., and Running, S. W.: Climate-driven increases in global terrestrial net primary production from 1982 to 1999, science, 300, 1560–1563, 2003.

Pastorello, G., Trotta, C., Canfora, E., Chu, H., Christianson, D., Cheah, Y.-W., Poindexter, C., Chen, J., Elbashandy, A., Humphrey, M., et al.: The FLUXNET2015 dataset and the ONEFlux processing pipeline for eddy covariance data, Scientific data, 7, 225, 2020.

Prein, A. F., Langhans, W., Fosser, G., Ferrone, A., Ban, N., Goergen, K., Keller, M., Tölle, M., Gutjahr, O., Feser, F., et al.: A review on regional convection-permitting climate modeling: Demonstrations, prospects, and challenges, Reviews of geophysics, 53, 323–361, 2015.

Pu, J., Chang, Y., Gao, S., Bao, S., Yan, K., Sun, X., Carvalhais, N., and Myneni, R. B.: MCI GPP: ensembling a global model- and climate-independent gross primary productivity for 2001–2023, Scientific Data, 12, 1965, https://doi.org/10.1038/s41597-025-06218-8, 2025.

Qian, H., Joseph, R., and Zeng, N.: Enhanced terrestrial carbon uptake in the Northern High Latitudes in the 21st century from the Coupled Carbon Cycle Climate Model Intercomparison Project model projections, Global Change Biology, 16, 641–656, 2010.

Running, S. and Zhao, M.: MODIS/Terra gross primary productivity gap-filled 8-day L4 global 500m SIN grid V061, NASA EOSDIS Land Processes Distributed Active Archive Center (DAAC) data set, pp. MOD17A2HGF–061, 2021.

Schaphoff, S., Lucht, W., Gerten, D., Sitch, S., Cramer, W., and Prentice, I. C.: Terrestrial biosphere carbon storage under alternative climate projections, Climatic change, 74, 97–122, 2006.

Schär, C., Fuhrer, O., Arteaga, A., Ban, N., Charpilloz, C., Di Girolamo, S., Hentgen, L., Hoefler, T., Lapillonne, X., Leutwyler, D., et al.: Kilometer-scale climate models: Prospects and challenges, Bulletin of the American Meteorological Society, 101, E567–E587, 2020.

Schneck, R., Gayler, V., Nabel, J. E., Raddatz, T., Reick, C. H., and Schnur, R.: Assessment of JSBACHv4. 30 as a land component of ICON-ESM-V1 in comparison to its predecessor JSBACHv3. 2 of MPI-ESM1. 2, Geoscientific Model Development, 15, 8581–8611, 2022.

Segura, H., Pedruzo-Bagazgoitia, X., Weiss, P., Müller, S. K., Rackow, T., Lee, J., Dolores-Tesillos, E., Benedict, I., Aengenheyster, M., Aguridan, R., et al.: nextGEMS: entering the era of kilometer-scale Earth system modeling, EGUsphere, 2025, 1–39, 2025.

Stevens, B., Acquistapace, C., Hansen, A., Heinze, R., Klinger, C., Klocke, D., Rybka, H., Schubotz, W., Windmiller, J., Adamidis, P., Arka, I., Barlakas, V., Biercamp, J., Brueck, M., Brune, S., Buehler, S. A., Burkhardt, U., Cioni, G., Costa-Suros, M., Crewell, S., Crueger, T., Deneke, H., Friederichs, P., Henken, C. C., Hohenegger, C., Jacob, M., Jakub, F., Kalthoff, N., Koehler, M., van Laar, T. W., Li, P., Loehnert, U., Macke, A., Madenach, N., Mayer, B., Nam, C., Naumann, A. K., Peters, K., Poll, S., Quaas, J., Roeber, N., Rochetin, N., Scheck, L., Schemann, V., Schnitt, S., Seifert, A., Senf, F., Shapkalijevski, M., Simmer, C., Singh, S., Sourdeval, O., Spickermann, D., Strandgren, J., Tessiot, O., Vercauteren, N., Vial, J., Voigt, A., and Zaengl, G.: The Added Value of Large-eddy and Storm-resolving Models for Simulating Clouds and Precipitation, Journal of the Meteorological Society of Japan, pp. 395–435, 2020.

Store, C. C. D.: Land cover classification gridded maps from 1992 to present derived from satellite observations, Copernicus Climate Change Service, pp. 7–9, 2019.

Sun, Y., Solomon, S., Dai, A., and Portmann, R.: How often does it rain?, 2005.

Tang, X., Fan, S., Du, M., Zhang, W., Gao, S., Liu, S., Chen, G., Yu, Z., and Yang, W.: Spatial and temporal patterns of global soil heterotrophic respiration in terrestrial ecosystems, Earth System Science Data, 12, 1037–1051, 2020.

Tuomi, M., Thum, T., Järvinen, H., Fronzek, S., Berg, B., Harmon, M., Trofymow, J., Sevanto, S., and Liski, J.: Leaf litter decomposition—Estimates of global variability based on Yasso07 model, Ecological Modelling, 220, 3362–3371, 2009.

Vetter, M., Churkina, G., Jung, M., Reichstein, M., Zaehle, S., Bondeau, A., Chen, Y., Ciais, P., Feser, F., Freibauer, A., et al.: Analyzing the causes and spatial pattern of the European 2003 carbon flux anomaly using seven models, Biogeosciences, 5, 561–583, 2008.

Wieners, K.-H., Giorgetta, M., Jungclaus, J., Reick, C., Esch, M., Bittner, M., Legutke, S., Schupfner, M., Wachsmann, F., Gayler, V., Haak, H., de Vrese, P., Raddatz, T., Mauritsen, T., von Storch, J.-S., Behrens, J., Brovkin, V., Claussen, M., Crueger, T., Fast, I., Fiedler, S., Hagemann, S., Hohenegger, C., Jahns, T., Kloster, S., Kinne, S., Lasslop, G., Kornblueh, L., Marotzke, J., Matei, D., Meraner, K., Mikolajewicz, U., Modali, K., Müller, W., Nabel, J., Notz, D., Peters-von Gehlen, K., Pincus, R., Pohlmann, H., Pongratz, J., Rast, S., Schmidt, H., Schnur, R., Schulzweida, U., Six, K., Stevens, B., Voigt, A., and Roeckner, E.: MPI-M MPI-ESM1.2-LR model output prepared for CMIP6 CMIP piControl, https://doi.org/10.22033/ESGF/CMIP6.6675, 2019.

Yuan, Q., Wang, X., Che, T., and Li, J.: Global carbon flux dataset generated by fusing remote sensing and multiple flux networks observation, Scientific Data, 12, 1359, https://doi.org/10.1038/s41597-025-05672-8, 2025.

Zhu, S., Xu, J., Zeng, J., Bao, S., Chen, Y., Shi, S., Zheng, Z., Dong, W., Wang, Y., and Shi, J.: The UFLUX ensemble of multiple-scale carbon, water, and energy fluxes, Scientific Data, 13, 90, https://doi.org/10.1038/s41597-025-06401-x, 2025.